Trends in excitonic, vibrational and polaronic properties of graphitic carbon nitride polymorphs

Ugolotti, Aldo[a], Di Valentin, Cristiana[a,*]

[a] *Dipartimento di Scienza dei Materiali, Università degli Studi di Milano-Bicocca, Via R. Cozzi 55, 20125, Milano, Italy*

Abstract

Although graphitic-carbon nitride (gCN) is a highly investigated inorganic semiconductor, especially in the field of photocatalysis, it is still the object of many controversial discussions. The possibility to easily synthesize a homogeneous heterostructure through the condensation and the polymerization of simple molecules allows the growth of a variety of structures with different electronic and optical properties. With the aim of driving the development of the catalyst towards improved performances or newer applications, it is paramount to understand the optically-driven excitation process within each polymer.

In this work, we focus on two models of melem-based gCN, i.e. the fully and the partially polymerized structures, and we perform a computational investigation, based on hybrid density functional theory calculations, of their optical properties in terms of vibrational and electronic excitations. First, we determine the normal modes of the ground state and we interpret the IR absorption spectrum. Then, we simulate the electronic excited state with an electron-hole pair model and we determine the exciton binding energy, the self-trapping energy and the photo-emission energy. We compare these numerical results with the experimental data available in literature and in addition we discuss the role of the different polymeric arrangements.

Keywords: g-C3N4, polymer, DFT, exciton, vibration, melon, melem

*corresponding author: cristiana.divalentin@unimib.it

https://doi.org/10.1016/j.apsusc.2022.155164

1. Introduction

Graphitic-carbon nitride (gCN) is a layered inorganic semiconductor, which is widely studied in the field of catalysis because of its low-toxicity, thermal stability and relatively cheap and simple synthesis[1, 2, 3, 4, 5, 6]. Its conformation exposing N-rich coordinating atoms and its electronic structure make gCN an interesting candidate for the application in sensing or biomedical devices[3] as well as an ideal platform for the embedding of transition metal atoms for single-atom heterogeneous catalysis[7, 8]. gCN is expected to catalyze a large variety of chemical reactions, such as water splitting, degradation of pollutants or selective transformation of organic compounds, which can be triggered by the irradiation with light at different wavelengths[2, 3, 9, 10, 11, 12, 13]. The possibility to use visible light makes it more interesting than other semiconducting materials that do not match the solar light spectrum. Additionally, the chemical activity of pristine gCN can be further tailored through several modifications[14, 15] and, among those, the inclusion of single metal or non-metal atoms is one of the most investigated[16, 17, 18, 19, 20, 21, 22]. Therefore, in order to understand the catalytic properties of gCN, it is extremely important to rationalize the dynamics of the charge carriers, which would mediate any photoactivated process.

Because of the polymeric nature of gCN, the actual structure and composition of a sample are dependent on the growth conditions, among which the chosen molecular precursor and the temperature are the most crucial. In the case of the melem monomer, object of the present study, it has already been shown that polymerization is only partial, as a Liebig's melon, rather than full, through all of its amino terminal groups[23, 24, 25, 26, 27].

From an experimental point of view, gCN is commonly characterized through optical spectroscopy: the IR window is analyzed in order to find the fingerprints of the functional groups present in the sample and therefore obtain indirect information about its morphology, while the excitonic properties are studied in the UV-vis range. Most of the IR studies agree on the observation of a strong similarity between the spectra recorded for the polymer and the monomer/precursor[19, 23, 28, 29, 30, 31], which suggests an incomplete polymerization, despite the sample being frequently modeled with an ideal fully-polymerized structure. The electronic absorption or the emission spectra present a direct transition at $\sim$ 2.7 eV with negligible or minimal Stoke shift at room temperature[19, 20, 29, 30, 31, 32, 33, 34, 35, 36].

https://doi.org/10.1016/j.apsusc.2022.155164

In some other works[1, 37, 38, 39, 40], time- or temperature-dependent spectroscopies are used to highlight the important role of the temperature, either during the sample growth or during the characterization.

Similarly, the existing theoretical and computational literature on the optical properties of gCN is rather confused, with still many open questions. On one side, the formation of excitons with few hundreds of meV of binding energy is expected from general considerations on semiconducting polymers[41, 42]. On the other side, the experimental findings of both faster ($\sim$ 1-5 ns) and slower ($\sim$ 15-40 ns) recombination times of the photo-induced electron-hole pairs[38, 40, 43, 44, 45, 46, 47] suggests the presence of more complex dynamical effects. In fact, the time decay of the photoemission profiles can be compared with analytical models assuming both the direct recombination of the excitons and the recombination of free charge carriers[38]. The band structure or the absorption spectrum of gCN are the most frequent targets of the computational investigations, but, however, they are calculated with a setup chosen to reproduce the experimental onset of the visible light absorption[16, 17, 21, 48]. This constraint annihilates the difference between the electronic and optical gap, thus neglecting any excitonic or polaronic effects. Additionally, even if more refined methods are considered, for example many-body perturbation theories, like solving the Bethe-Salpeter equation (BSE), or time-dependent density functional theory (TD-DFT), the model structure is either too constrained[49, 50], i.e. symmetrical or flat, or too simplified[50], i.e built as a non-periodic cluster, therefore hampering a direct comparison with actual gCN polymers in real samples. Little attention has been paid to the number of simulated layers, which can play an important role in determining the excitonic binding strength, because of a reduced screening in an exfoliated two-dimensional layer with respect to a bulk multilayered heterostructure[51, 52]. Finally, only the out-of-plane electron-hole correlation is commonly discussed and reported[39, 53], which, however, should have a minor impact on the actual properties of gCN, given the generally accepted picture of weakly interacting layers stacked in bulk samples[26]. In-plane effects should also be evaluated because they could play a crucial role.

In this work, we perform an ab-initio investigation of the electronic, optical and vibrational properties of melem-based gCN models that are commonly proposed in the analysis of experimental samples. With respect to previous studies, we remove all structural constraints and we employ both a different density functional with some exact exchange and a more state-of-

https://doi.org/10.1016/j.apsusc.2022.155164

the-art correction for the dispersion interactions (B3LYP[54, 55]+Grimme-D3[56]). We simulate IR spectra, band structures and exciton binding energies for different periodic arrangements of the monomer and we discuss the similarities with the melem monomer itself. We evaluate the excitonic properties of 2D and 3D gCN models using an hydrogen-like model, with the addition of the contribution of the ionic lattice vibrations to the dielectric response. For the 2D systems, since the dielectric constants are not known, we estimate them through two different numerical approaches, based on the treatment of the 2D sheet as an ideal two-dimensional layer[57, 58] or as a plate of a capacitor[59, 60], which we then compare. Finally, we analyze our results with reference to available experimental data in order to provide a rationale in the analysis of the properties of actual samples.

2. Computational Methods

All ground state calculations were performed within the DFT framework using the CRYSTAL17 package[61, 62], with an all-electron basis set of Gaussian-type orbitals as (C) 6-311(d1), (N) 6-311(d1), (H) 3-11(p1)[63]. We used the B3LYP hybrid functional[54, 55] and we accounted for the dispersion interaction by including the Grimme D3 algorithm[56]. The fully relaxed supercells were constructed including four monomers, to ensure proper optimization constraints; the reciprocal space was mapped through a grid of 4 k-points along each periodic direction, generated by the Monkhorst-Pack algorithm. For selected models, we performed additional calculations using the HSE06[64, 65] (for structural optimization and band structure calculations) and the PBE0[66] (for dielectric response calculation) hybrid functionals.

The cases in which a single electron or hole was added to the ground state model were dealt with the addition of a uniform background in order to enforce the neutrality of the supercell, while a spin-doublet solution was imposed. When an electron-hole pair was considered, the system was kept neutral, but the solution was constrained into a triplet spin state. The self-trapping of the charge carriers was simulated by optimizing the structures while constraining the charge and spin state of the system just as discussed. This approach represents indeed an approximation for the actual first excited state, which should be a spin-singlet; however, such a methodology has been already successfully employed in the study of other semiconductors, like TiO_2[67] or WSe_2[68].

https://doi.org/10.1016/j.apsusc.2022.155164

The vibrational properties of the neutral ground state, i.e. the frequencies and displacements of the normal modes, were calculated within the harmonic approximation as implemented in CRYSTAL17; the IR spectra were generated by the convolution of the calculated peaks with Gaussian line profiles broadened with σ=15 cm^{-1}.

The binding energy of the exciton ($\mathrm{E_{bind}}$) in two-dimensional models was calculated through the hydrogenic approximation[69], for an in-plane excitation only. Indeed, this component is the least affected by dimensionality effects, i.e. the reduced electron screening, but the perturbation perpendicular to the plane in two-dimensional systems is intrinsically microscopic, and we deem it not suited for being consistently paired with a more macroscopic approach such as the hydrogen-like model. Therefore, we considered:

$$\mathrm{E_{bind}} = \frac{4m_r^*}{\epsilon_{2D}^2}\mathrm{E}_H \tag{1}$$

$$\frac{1}{m_r^*} = \frac{1}{m_e^*} + \frac{1}{m_h^*} \tag{2}$$

where E_H is the Rydberg energy unit and m_r^* is the reduced mass of the exciton, calculated from that of the electron (m_e^*) and the hole (m_h^*). These two values were calculated by fitting the highest occupied and the lowest unoccupied bands with parabolic functions:

$$\varepsilon(\mathbf{k}_i) = \varepsilon_0(\mathbf{k}_0) \pm \frac{\hbar^2}{m_{e,h}^*}(\mathbf{k}_0 - \mathbf{k}_i)^2 \tag{3}$$

around their respective minimum energy $\varepsilon_0(\mathbf{k}_0)$, along an user-defined direction in reciprocal space $\mathbf{k}_i$. The dielectric constant of the two-dimensional layer ϵ_{2D} was evaluated from the macroscopic one ϵ_{SC}, calculated for the fictitious three-dimensional supercell through two different approaches which are frequently found in literature.

One is based on the analytic treatment of the reduced screening of a charge confined in an ideal sheet represented by a Dirac delta[57]. The resulting dispersion relation of the dielectric function is averaged on an effective sphere with radius equal to Bohr radius to obtain an effective dielectric constant[58]:

$$\epsilon_{2D} = \frac{8m_r^*}{\left(1 + \sqrt{1 + 32\pi\alpha_{SC}L_z/3}\right)^2} \tag{4}$$

https://doi.org/10.1016/j.apsusc.2022.155164

where α_{SC} is the polarizability calculated in the supercell setup, with height L_z in the non-periodic direction[57].

The second approach we considered for the evaluation of ϵ_{2D} is based on the effective medium approximation: in this case the periodically repeated slabs are treated as a capacitor made of dielectric plates separated by vacuum[59, 60]; therefore it is possible to define the in-plane dielectric constant as:

$$\epsilon_{SC} = 1 + \frac{\delta_z}{L_z}(\epsilon_{2D} - 1) \tag{5}$$

After performing the calculations of ϵ_{SC} for several supercells with different size, the actual electronic thickness δ_z and the two-dimensional dielectric constant are obtained by fitting the data with the equation above.

Through the hydrogenic approximation, we can evaluate the contribution of the polaronic response of the ion cores of the atoms to the polarizability. In fact, in a perturbative scheme, the total dielectric function can be written as $\epsilon = \epsilon_{opt} + \epsilon_{vibr}$, i.e. the sum of an optical and a vibrational contribution, respectively. While the latter is calculated after the vibrational spectrum[70], the former is calculated with the coupled-cluster Kohn-Sham approximation[71, 72, 73].

In case of a bulk calculation, the binding energy is calculated in a similar way as the two-dimensional system, but the factor 4 in Equation 1 is dropped and the dielectric constant is taken directly from the supercell calculation. The reduced mass is calculated from the parabolic fit of the highest occupied and the lowest unoccupied bands considered for the whole first Brillouin zone, i.e. also accounting for the dispersion along the stacking direction of layers.

For the melem monomer only, the hydrogenic approximation cannot be applied because of the non-periodic nature of the calculation. Therefore, in order to estimate the excitonic binding energy of the molecule, the properties of its excited states were calculated using the GAUSSIAN package[74], within the TD-DFT framework, using the B3LYP exchange and correlation functional and a 6-311++(d,p) atomic-centered Gaussian basis set: in this case the excited state can be properly simulated as a spin singlet.

https://doi.org/10.1016/j.apsusc.2022.155164

3. Results and Discussion

3.1. Melem monomer

Ground state structure and properties. Given the importance of melem as the building block of the polymers structure, we first present the ground state properties of a single isolated molecule, which can be considered as a reference. The molecular and electronic structures are reported in Figure 1a,b: the calculated HOMO-LUMO gap is 4.91 eV; the electrons in the HOMO state are localized on the p_z orbitals of the pyridinic N atoms, while the LUMO is shaped as a fully delocalized Π^* state.

https://doi.org/10.1016/j.apsusc.2022.155164

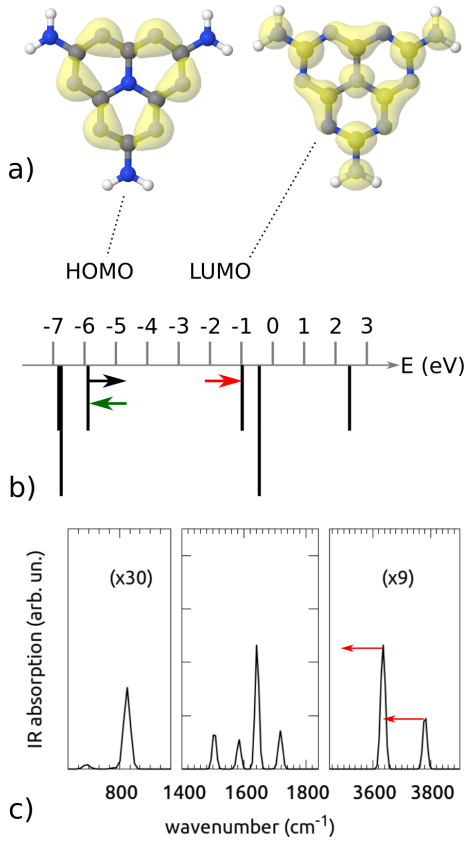

Figure 1: Ground state configuration of the melem monomer: (a) charge distributions of HOMO and LUMO orbitals and (b) energetic scheme of the frontier molecular orbitals (MOs). The arrows in scheme (b) highlight the MO to which a single electron added to the system (red) or the one to which it is removed (green) in order to simulate a hole. The black arrow represents the "spectator" electron. The C, N, H atoms are shown with gray, blue, white spheres; isovalues 0.02 e/Å^3. The calculated IR absorption spectrum is reported in panel c: the red arrows show the red-shift estimated through anharmonic corrections.

Starting from this optimized structure, we calculated the IR absorption spectrum, which is reported in Figure 1c, where three populated regions can be identified, in good agreement with both experimental and theoretical results already reported in literature[28]. Starting from the lowest energy side of the spectrum, in the first region a major feature at $\sim 815\,\mathrm{cm}^{-1}$ is observed. The analysis of the dislocations of the corresponding normal modes, shown in Figure SI1, associates this mode with the anti-phase oscillation, out of the σ_h plane of the molecule, of the C and N atoms. The most absorbing

https://doi.org/10.1016/j.apsusc.2022.155164

vibrational modes are found in the second region of the calculated spectrum, in the frequency range between 1400-1600 cm^{-1}. These features correspond to the combination of the scissor or rocking motions of the atoms in the amino group with the stretching or bending of N-C bonds. Lastly, at the highest end of the calculated spectrum, in the third region, two main features are observed, at $\sim$ 3635 cm^{-1} and $\sim$ 3778 cm^{-1}, which we assign to the combination of stretching motions of the N-H_2 bonds. Such modes, however, are known to suffer from anharmonic effects and, in fact, the agreement with the experimental values is less good, since the same modes have been recorded at 3428 and 3488 cm^{-1}[28]. Therefore, we have estimated the error due to the harmonic approximation through a dedicated module in the code[75, 76], which allows to compute a scaling factor (here 0.96) that can be used to correct the frequencies above to 3491 and 3627 cm^{-1}. These corrected values, although not perfectly matching the experimental data because of the crudeness of the scaling method, still allows us to obtain a qualitative understanding of the vibrational properties of the system.

Excited state structure and properties. The investigation of the excitation process was performed step-by-step, as schematically represented in Figure 2a. First, we obtained the (first) vertically excited triplet state (T_1[GS], where [GS] indicates the geometry of the molecule is still that of the optimized ground state), from which we can evaluate the vertical absorption energy, E_{abs}=E(T_1[GS])-E(S_0[GS]). We used the total energy from DFT calculations, which is a ground-state theory, because T_1 is formally a ground state for the spin triplet multiplicity. This is clearly a spin-forbidden excitation but we expect it to highly resemble the S_0[GS] $\rightarrow$ S_1[GS] excitation that we cannot compute in this simplified approach. As a second step, we fully relaxed the T_1 structure to simulate the exciton self-trapping, obtaining the energy minimum (T_1[Ex]) state and derived the exciton self-trapping energy as E_{st}=E(T_1[Ex])-E(T_1[GS]). Using the same atomic configuration, we calculated the distorted ground state energy for S_0[Ex] and the polaronic distortion energy, E_{dist}=E(S_0[GS])-E(S_0[Ex]). Finally we derived the photoemission energy as E_{pl}=E_{abs}+E_{st}+E_{dist}.

There are, however, additional physical quantities involved in the picture described above that have to be carefully evaluated: the most important is indeed the exciton binding energy, which is not guaranteed to be included in the calculation of polaronic effects[68]. If we remove the polaronic contributions of the two isolated charge carriers (of the photoxcited electron, E^e_{st}, and of the photoexcited hole, E^h_{st}) from the exciton self-trapping energy,

https://doi.org/10.1016/j.apsusc.2022.155164

we can isolate the interaction energy of the e-h pair. These contributions are evaluated by constructing the charged ground state and calculating the energy difference before and after the optimization of the atomic structure, as described in the next paragraph.

First, one extra electron o extra hole is added to the molecule and the total wavefunction is relaxed; then, the atomic structure in the charged state is optimized to assess the polaronic distortion and energy. The charge distributions for the systems with an extra electron and an extra hole, shown in Figure 2b, correspond, as expected, to that of the LUMO and that of the HOMO of the neutral molecule (Figure 1b), respectively.

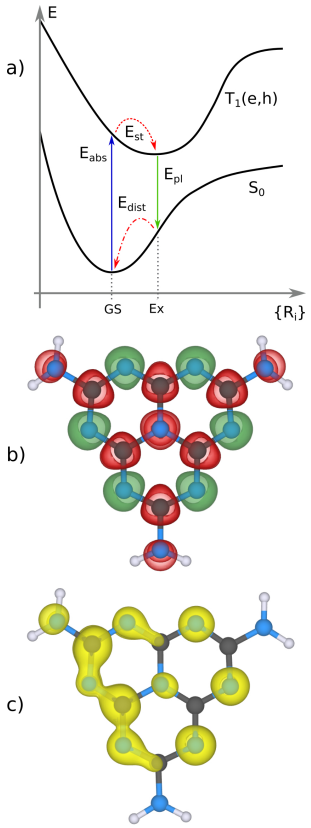

Figure 2: Panel (a) reports a sketch of the structure, in the configuration space, of the ground (S_0) and excited (T_1) state, the latter including an electron-hole pair (e,h). Panel (b,c) Charge distribution of the melem molecule with the addition of a single electron(red)/hole(green) (b) and of an (e,h) pair (c): isovalues 0.02 e/Å^3; the C, N, H atoms are shown with gray, blue, white spheres.

https://doi.org/10.1016/j.apsusc.2022.155164

In addition to these total energy calculations based on DFT considering the T_1 excited state, we have also performed some TD-DFT calculations, as described in Section 2, for the S_1 excited state. In Table 1 we collected all the energy terms calculated with the two methods for direct comparison: the absorption and the binding energies are rather similar, confirming that using the T_1 state as the analogous of the true first excited state S_1 is a viable and acceptable approximation. Our results for the HOMO-LUMO gap are in agreement with the experimental excitation peak at 4.30 eV observed at room temperature[28]. The DFT and TD-DFT methods differ, however, on the strength of the self-trapping, as the DFT optimization of the triplet state overestimates E_{st} and E_{dist} and, consequently, reduces the photoemission energy; interestingly, the DFT value is in better agreement with the experimental peak at 3.39 eV[28]. We note that the self-trapping energy of the exciton is quite smaller than that for the isolated electron or for the isolated hole, indicating an additional interaction of the two polarons, which is also suggested by the less symmetric charge density of the exciton, shown in Figure 2c, compared with that of the isolated polarons (Figure 2b).

Table 1: Excited state properties of the melem monomer, calculated by two different methodologies: the optimization of the triplet state (DFT) and the optimization of the singlet state (TD-DFT). Note: * the binding energy is calculated here as the difference between the HOMO-LUMO gap and the absorption energy.

(eV)	DFT(T_1)	TD-DFT(S_1)
E_{gap}	4.91	4.99
E_{abs}	3.88	3.86
E^*_{bind}	1.03	1.13
E_{st}	−0.19	−0.06
E_{dist}	−0.36	−0.06
E_{pl}	3.34	3.74
E^e_{st}	−0.41	-
E^h_{st}	−0.08	-

3.2. Ideal 2D Graphitic Carbon Nitride

Ground state structure and properties. From the single melem monomer we now move to the extended polymeric systems by considering first the most regular two-dimensional fully-polymerized gCN (igCN). This polymer could be modeled as flat, as often previously done, but it is ac-

https://doi.org/10.1016/j.apsusc.2022.155164

tually more stable in the buckled form, which we have already discussed elsewhere[27] and is shown in Figure 3a. We must point out that, because of the aggregation of the monomers, no amino N (N amino) atoms are left in igCN. We can distinguish here three types of N atoms: N atoms joining the monomers (N joint), pyridinic N species (N pyridinic) and N atoms at the center of the molecule (N center). The asymmetric corrugation along the x or y axis breaks the symmetry of the ideal crystal, which is confirmed by the presence of two, now not equivalent, high-symmetry paths in the band structure reported in Figure 1b. The calculated band gap is 3.03 (direct) eV at the K point. The states at the top and at the bottom of the valence and the conduction band, whose charge densities are reported in Figure 3a, do not differ from the HOMO and the LUMO, respectively, of the isolated monomer (Figure 1b). Similarly, the analysis of density of states (DOS) of the polymer (Figure 3c) suggests that the top of the valence band is localized on pyridinic N atoms, while the bottom of the conduction band is composed of Π^* states.

The IR absorption spectrum of the 2D layer calculated from the optimized, corrugated structure is reported in Figure 3d: the most striking difference from that of the monomer is the absence of any absorption at energies higher than 1800 cm^{-1}. This is expected, however, based on the fact that such normal modes are exclusive to stretching displacements along N-H bonds in NH_2 groups, as detailed above. The investigation of the displacement for each individual mode, shown in Figure SI2, reveals a similarity between igCN and the monomer: the lower energy end of the spectrum is composed of out-of-plane displacements, which are retained despite the corrugation of the layer, while the absorption between 1100 and 1800 cm^{-1} is due to the overlap of modes involving either N center, N joint or N pyridinic without a recognizable order.

https://doi.org/10.1016/j.apsusc.2022.155164

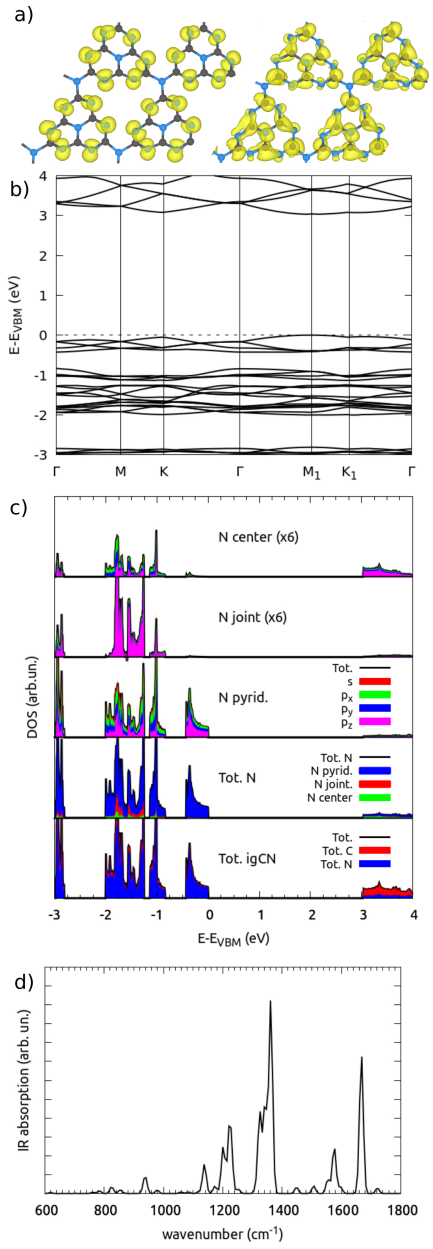

Figure 3: Properties of the ground state of 2D igCN. (a) top view of the charge distributions of the topmost valence (left) and bottommost conduction (right) states within the supercell. Isovalues 0.02 e/Å^3; C, N atoms are shown with gray, blue spheres. (b, c) band structure and density of states, projected onto atomic orbitals. The energies are reported with respect to the valence band maximum (VBM). (d) IR absorption spectrum.

https://doi.org/10.1016/j.apsusc.2022.155164

Excited state structure and properties. In order to construct the lowest lying triplet exciton state (T_1), we have considered different possible configurations for the position of the photoexcited electron and the photoexcited hole in the supercell and determined the one with the lowest energy. From the band structure reported in Figure 4a, in analogy with what observed for the monomer, in igCN the electron is localized on a LUMO-like state at the bottom of the conduction band, while the hole is localized on a HOMO-like state at the top of the valence band (see Figure SI3 for the inclusion of a single electron/hole). The polaronic optimization of T_1 slightly increases the corrugation of the layer as the repulsion between the adjacent monomers intensify, but the displacements are smaller than 0.05 Å, as it is shown in Figure SI4. These results are in contrast with the charge density of the cation of melem dimer proposed by Meek et al.[50] where the hole is centered around the N joint atom. We deem such a difference due to several factors, the most important of which is geometrical: a non-periodic configuration allows for lower corrugation, reducing the repulsive N-N interactions through displacements within the plane in which the molecule lies. As it will be shown below, a flat igCN presents rather different properties than its buckled counterpart.

Interestingly, while the separated charge carriers are somehow spread on all the four monomers in the supercell (Figure SI3a), the exciton is localized on a single melem unit, as shown in Figure 4b, which suggests that the electron-hole pair is electrostatically bound. We observe such confined behavior even before optimization of the T_1 state (not shown here); therefore, we expect that our first approach, i.e. the evaluation of the polaronic self-trapping, will not account for the binding energy of the exciton, which we need to evaluate through a different approach, i.e. using the hydrogenic approximation (see Equation 1).

https://doi.org/10.1016/j.apsusc.2022.155164

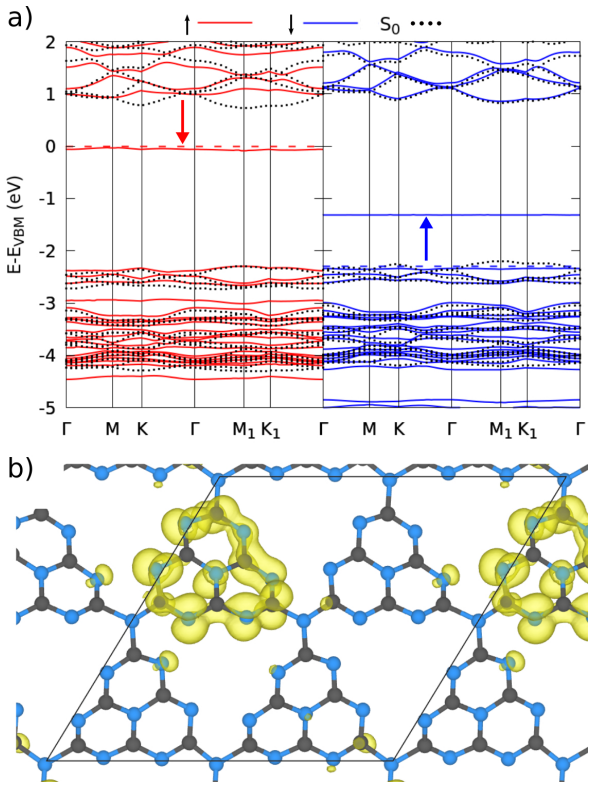

Figure 4: Electronic properties of the optimized triplet exciton in 2D igCN: (a) spin-resolved band structure, (b) charge density distribution. In panel a, the ground state band structure is reported as well (S_0, black dots) for comparison, by aligning the least perturbed bands. The energies are referred to the valence band maximum (VBM). The arrows highlight the state getting filled in (red arrow) and that getting emptied (blue arrow). Isovalues 0.02 e/Å^3; C,N atoms are shown with gray, blue spheres.

The first term of Equation 1 that we are going to discuss is the reduced effective mass. To evaluate it, we consider the representation of the eigenvalues in the reciprocal space for the topmost state in the valence band and the lowest one in the conduction band, as shown in Figure 5 and we perform the fit, around the K point, with isotropic parabolic functions (Equation 3). The results are collected in Table 2 the effective masses are in good agreement with those calculated for a bulk model of igCN [51], despite the rather different band structure: the reported band gap is 2.8 eV at the Γ point. We deem such a discrepancy to be related to both the different exchange-correlation functional, HSE06 rather than B3LYP, and the different supercell structure, orthorhombic rather than hexagonal-like.

https://doi.org/10.1016/j.apsusc.2022.155164

The type of representation introduced above is also helpful in clarifying some details of the electronic structure of the ground state: the band gap is clearly located at the K point only in the reciprocal space, while additional minima that could be observed in the band structure (Figure 3b), for example at the M point, are only apparent ones, generated by the repetition of the crystal structure and the proximity to the K point.

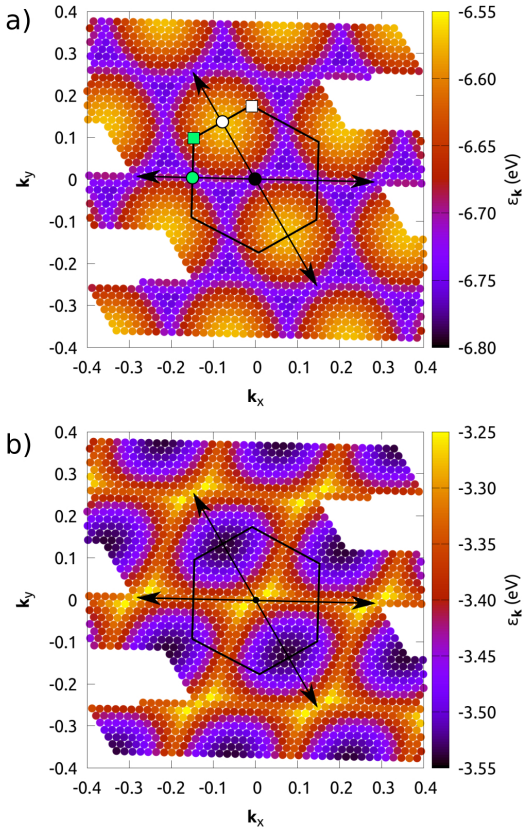

Figure 5: Reciprocal space representation of the eigenvalues of the highest occupied states (panel a) and the lowest empty ones (panel b) of 2D igCN. The structure of the first Brillouin zone and that the crystal are shown as well. Panel (a) reports the most important high-symmetry points, included in the band structure calculation: Γ (black dot), M (white dot), K (white square), M_1 (green circle), K_1 (green square)

The hydrogenic model is extremely sensitive to the dielectric function, which in turn is expected to vary sensibly when the dimensionality of the system is reduced, as in the case of exfoliated sheets. Since there is no

https://doi.org/10.1016/j.apsusc.2022.155164

definitive approach to evaluate unambiguously a macroscopic quantity, such as ϵ, in a microscopic system (i.e. a non-periodic system, at least in one direction), we decided to determine the two-dimensional dielectric constant, to be used in Equation 1 to estimate the exciton binding energy, through two different approaches: in the first case we pursue an analytic solution, while, in the second one, we rely on the fit of a capacitance model (see Section 2 for additional references).

Table 2: Excited state properties of 2D igCN as obtained in this work and of 3D igCN as reported in Ref.[51].

	This work		Bulk-HSE06[51]
m_e^*	0.75		0.4
m_h^*	1.03		1.4
m_r^*	0.43		0.3
	ϵ_{2D} analytic	ϵ_{2D} fit	
ϵ	3.9	5.5	7.2
ϵ_{opt}	3.2	4.3	5.0
E_{bind} (eV)	1.56	0.79	0.33
E_{bind}^{opt} (eV)	2.35	1.26	0.68
E_{gap} (eV)	3.03		2.8
E_{abs} (eV)	2.72		-
E_{st} (eV)	-0.20		-
E_{dist} (eV)	-0.38		-
E_{pl} (eV)	2.14		-
E_{st}^{e} (eV)	-0.08		-
E_{st}^{h} (eV)	-0.03		-

The analysis of the values of the ϵ reported in Table 2 reveals two opposite trends: the first one is the reduction of the dielectric constant, up to 46% for a perfectly 2D charge distribution, given by the reduced electronic screening taking place in the single layer compared with that of a three-dimensional structure (results from Ref.[51]). However, given the significant corrugation of the igCN structure, we have evaluated the dielectric constant also through a more macroscopic model, i.e. using the effective medium approximation. In this case, the value of ϵ is larger than that of the analytic model and, although, it gets closer to the value reported for the bulk system[51], it is

https://doi.org/10.1016/j.apsusc.2022.155164

still 24% smaller. A second trend is the increase of the values of ϵ given by the contribution of the ionic response to the perturbing electric charge, which is of the order of $\sim$ 20% of the total, almost independent from the dimensionality of the system.

As a consequence, the binding energy of the exciton of an exfoliated layer is more than doubled with respect to that reported for the stacked layers[51], which agrees with the strongly bound excitons, with E_{bind} in the range of 1.3-2.2 eV, predicted for two-dimensional layers using BSE calculations[49, 77]. Finally, we observe that for the 2D igCN, the polaronic self-trapping and the distortion energies of the exciton are similar to those of the isolated monomer and are of the same order of magnitude of those calculated for the melem hexamer[50].

In the following we analyze how the results on the reduced effective mass, on ϵ and on the exciton binding energy vary depending on the computational setup, i.e. the exchange and correlation functional or the geometrical structure and other eventual constraints. For example, most of the computational results available in literature are calculated through the HSE06 functional[16, 17, 21, 48], which is chosen because the band gap predicted with it is in good agreement with the measured optical absorption peak at $\sim$ 2.7 eV, therefore neglecting the additional excitonic and polaronic interactions. In this case, the 2D igCN model has a rather similar electronic structure (Figure SI6a-c) and its values of the effective masses m_e^*=0.74, m_h^*=1.01 are almost identical to those calculated with B3LYP functional in the present work; the only difference is the magnitude of the band gap, which is smaller (2.84 eV vs 3.03 eV). Additionally, the evaluation of the dielectric constant, for example through the analytic model, produces values very close to those reported here for B3LYP (ϵ=3.8, E_{bind}=1.62 eV). Similarly, E_{st}=$-$0.15 eV and E_{dist}=$-$0.34 eV are in close agreement with B3LYP results.

For comparison, we also optimized a model of igCN, which has been constrained to be flat, in order to resemble the structure proposed by Wei and Jacob[39], using the same HSE06 exchange-correlation functional. Our results show the same exciton charge distribution reported in Ref.[49], which is centered around the N joint atom (not shown here) and is clearly different from what observed for corrugated igCN. Also, the band structure of the ground state of flat igCN (see Figure SI5c) is characterized by flatter conduction band minimum (CBM) and valence band maximum (VBM) bands than those of corrugated layer. Correspondingly, we calculated a much larger m_h^*, 1.92 instead of 1.03 and a slightly smaller m_e^*, 0.56 instead of 0.75. How-

https://doi.org/10.1016/j.apsusc.2022.155164

ever, the overall reduced mass is the same as for the corrugated igCN and the excitonic and polaronic results are almost identical, except for a slightly smaller E_{abs}, i.e. 2.59 instead of 2.72 eV.

As a final alternative model, we optimized a bulk model with AB stacked layers, whose geometry is reported in Figure SI5e. In this case, the inter-layer interaction is not negligible[27], as confirmed by the band structure details, shown in Figure SI5f: taking the whole three-dimensional crystal structure, the band gap is still ~ 3.0 eV but it is now indirect (always around Γ in the $\mathbf{k}_x$-$\mathbf{k}_y$ plane, but at different $\mathbf{k}_z$ coordinates). We have first investigated the possibility to obtain a bound electron-hole pair with the photoexcited charge carriers delocalized on adjacent igCN layers, as proposed in some studies[38, 39]. However, even without any polaronic relaxation, the exciton is formed on the single layer, which allows us to compare the absorption and self-trapping properties of the bulk to those of the isolated layer. Additionally, we investigated the optical dielectric constant of the system in the case of the direct Γ-Γ transition, which does not require any further processing, and the values of ϵ_{opt}=5.12 and E_{bind}^{opt}=0.90 eV are in agreement with those reported in literature for HSE06[51], despite the effective masses being "locally" different, i.e. m_e^* =1.70, m_h^* =0.82, but m_r^* =0.55 overall.

Within the limits of the two approaches we employed in this study, the binding energy of the excitons in the exfoliated layers of fully polymerized gCN is evaluated to be much larger than the thermal energy available at room temperature. Therefore, large energy differences are expected between the position of the onset and that of the maximum of the optical absorption spectra (assuming direct transitions only, as indirect channels which are not accounted for in our study). Additionally, the self-trapping energies and distortion should contribute to a measurable Stoke-shift. Notably, temperature-resolved UV-vis absorption spectra seem to confirm our hypothesis: binding energies in the range of 0.3-0.5 and Stoke-shifts $\sim$ 0.4-0.5 eV can be extrapolated from the reported data[32, 37, 38, 78].

3.3. Alternated melon 2D

Ground state structure and properties. Experimental evidences exist that full polymerization of precursors is not commonly achieved[25, 37, 38]. Therefore, we now consider models of partial polymerization of melem monomers. Since at least two 2D configurations can be constructed[27], we will focus on Liebig's or alternated melon structure. From its geometry and its band structure shown in Figure 6, it is possible to observe the presence of

https://doi.org/10.1016/j.apsusc.2022.155164

a preferential direction, i.e. the y axis of the cell, along which the polymerization takes place. The states at the top of the valence band and those at the bottom of the conduction one are similar to those of the HOMO and the LUMO of the isolated molecule (Figure 1b), although with a reduced charge density on N amino atoms. The calculated band gap is direct at the Γ point (3.90 eV), which is larger than that of the 2D igCN (3.03 eV).

https://doi.org/10.1016/j.apsusc.2022.155164

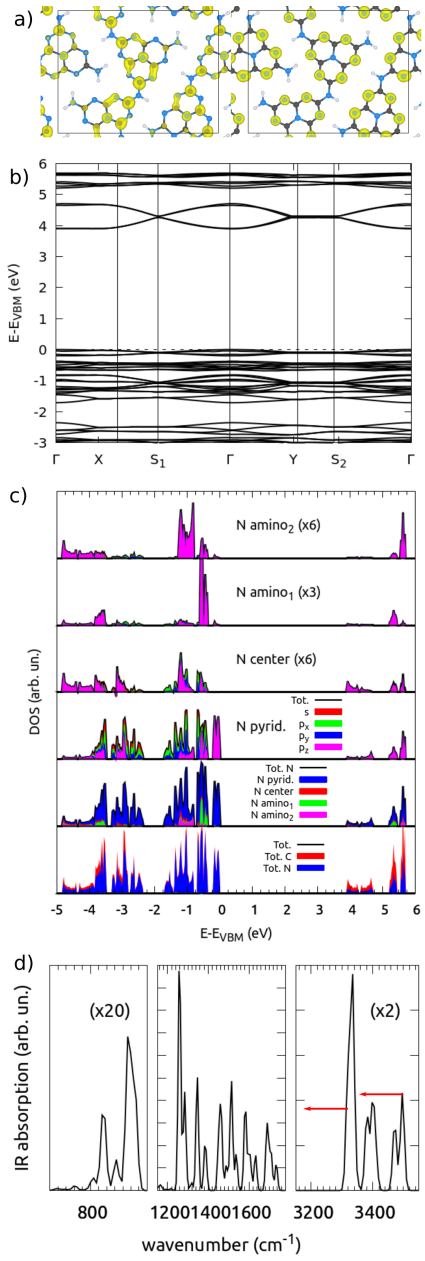

Figure 6: Properties of the ground state of 2D alternated melon: (a) top view of the charge distributions of the topmost valence (left) and bottommost conduction (right) states within the supercell. Isovalues 0.02 e/Å^3; C, N atoms are shown with gray, blue spheres. (b, c) band structure and density of states, projected onto atomic orbitals. The energies are reported with respect to the valence band maximum (VBM). (d) IR absorption spectrum: for energies around 3400 cm^{-1}, we report with red arrows the shift given by anharmonic corrections.

https://doi.org/10.1016/j.apsusc.2022.155164

The IR absorption spectrum, calculated from the optimized ground state, is shown in Figure 6d: as in the case of the monomer, three regions can be observed. Through the analysis of the displacements of the normal modes, shown in Figure SI6, it is possible to attribute the low energy end of the spectrum, around 800 cm^{-1}, to the out-of-plane distortion of the core of the monomers. At intermediate energies, from $\sim$ 1200 cm^{-1} to 1800 cm^{-1}, the normal modes involve mainly the bending of the atoms in amino groups (both primary and secondary) with the superposition with stretching displacements around N-C bonds. Lastly, for energies above 3000 cm^{-1} there are the stretching modes of the N-H_x bonds, which were clearly not present for the 2D igCN. In order to account for the anharmonicity of these modes, we report in the spectrum also the corrected energies of these vibrations, by rescaling the values with a coefficient of 0.96, similarly to what we have done for the monomer.

Excited state structure and properties. In this case of partial polymerization, the charge densities of the ground state including an additional single electron or hole, shown in Figure SI7a, are less localized on the amino groups than in the case of the monomer, suggesting a minor role played by the hydrogen bonds between adjacent rows of polymerized molecules. However, we note that the additional charges do not perturb much the band structure of the ground state (see Figure SI7b,c), similarly to what we observed for the igCN (see Figure SI3b,c). Therefore, upon the formation of the electron-hole pair, the resulting exciton is localized on a single monomer of the chain in the periodic system, where the electron occupies a state that resembles the LUMO of the molecule and the hole occupies a state that resembles its HOMO (see Figure 7), which is similar to what observed for 2D igCN.

https://doi.org/10.1016/j.apsusc.2022.155164

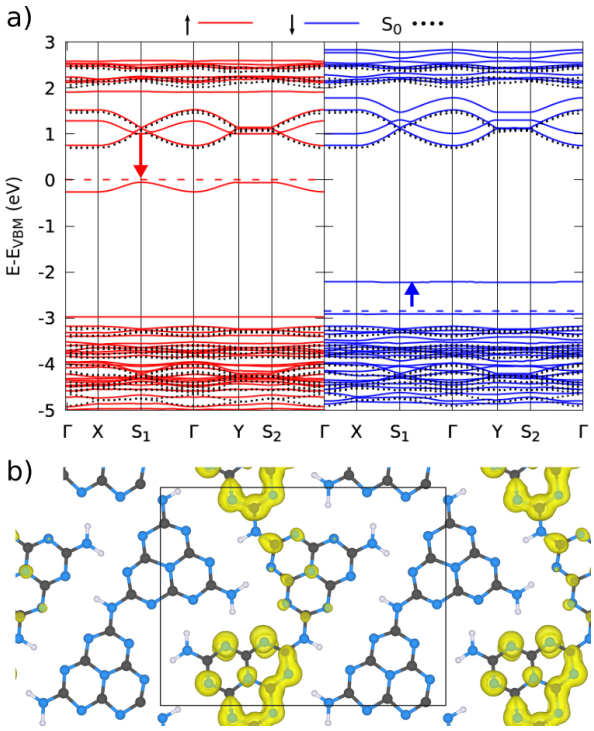

Figure 7: Electronic properties of the exciton of 2D alternated melon: (a) spin-resolved band structure, (b) charge density distribution. In panel a, the ground state band structure is shown (S_0, black dots) for comparison, by aligning the least perturbed bands. The energies are reported with respect to the valence band maximum (VBM). The arrows highlight the state getting filled (red arrow) and that getting emptied (blue arrow). Isovalues 0.02 e/Å^3; C, N and H atoms are shown with gray, blue and white spheres.

From the representation in the reciprocal space of the states around the band gap, shown in Figure 8, we can extract the effective masses for 2D alternated melon by fitting with the parabolic functions in Equation (3). In this case here, we restrict the fit to k-point differences along the $\mathbf{k}_y$ axis only, because it is the main polymerization direction. The results are collected in Table 3: all the effective masses are much different from those we have previously calculated for 2D igCN (see Table 2), which is a direct consequence of the different atomic configuration of the polymer, and also from those of a bulk melon model taken as a reference, despite the similarity with the reported band structure[51].

https://doi.org/10.1016/j.apsusc.2022.155164

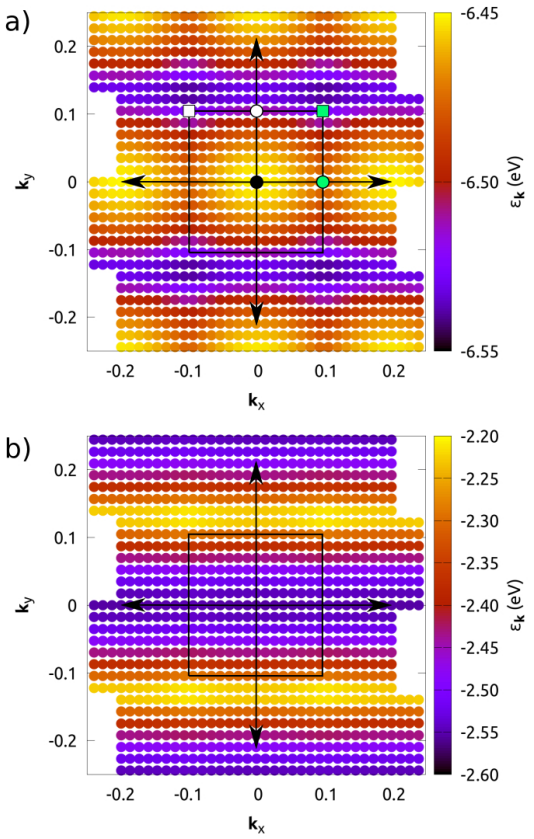

Figure 8: Reciprocal space representation of the eigenvalues of the highest occupied state (panel a) and the lowest empty one (panel b) of the 2D alternated melon. The structure of the first Brillouin zone and the crystal are shown as well. Panel a reports the most important high-symmetry points, included in the band structure calculation: Γ (black dot), X (green dot), S (green square), Y (white circle), S_1 (white square).

https://doi.org/10.1016/j.apsusc.2022.155164

Table 3: Excited state properties of the 2D alternated melon, as obtained in this work and of 3D igCN as reported in Ref.[51]. Notes: * calculated along the y-axis only.

	This work*		Bulk-HSE06[51]
m_e^*	0.31		0.9
m_h^*	1.32		1.6
m_r^*	0.25		0.6
	ϵ_{2D} analytic	ϵ_{2D} fit	
ϵ	2.7	5.0	6.1
ϵ_{opt}	2.4	4.0	4.1
E_{bind} (eV)	1.60	0.54	0.84
E_{bind}^{opt} (eV)	2.30	0.85	1.88
E_{gap} (eV)	3.90		3.4
E_{abs} (eV)	3.39		-
E_{st} (eV)	-0.17		-
E_{dist} (eV)	-0.27		-
E_{pl} (eV)	2.95		-
E_{st}^{e} (eV)	-0.06		-
E_{st}^{h} (eV)	-0.00		-

If we focus the attention on the dielectric constant, the values show similar trends to those we discussed above for 2D igCN, i.e. a reduction of ϵ with respect to bulk model and the important contribution of the ionic polarizability toward the electronic response of the system. Nonetheless, the values for the exciton binding energies are not as large as those for the fully polymerized case, because of the difference in the effective masses. The polaronic relaxation is slightly reduced compared to that of 2D igCN, which is a direct consequence of the different structure of the melon polymer, where the monomers are less tightly packed and the electrostatic repulsion is, thus, smaller.

Also in the case of 2D melon, the comparison with experimental data is difficult, because of the scarcity of studies on exfoliated polymers. Indeed, the similarity with the igCN would suggest the observation of both excitonic and polaronic effects, even at room temperature and stronger than those for samples containing stacked heterostructures. The only difference which would permit to clearly distinguish one polymer from the other by optical analysis is the higher band gap of the 2D melon compared to that of igCN,

https://doi.org/10.1016/j.apsusc.2022.155164

resulting in the shift towards higher energies of the spectral features, i.e. the peak and the onset of the adsorption and the peak of photoemission.

Experimental evidence shows that melon is a more common polymer in actual samples[26, 27], i.e. through XRD and XPS signatures, therefore we are tempted to look for similar fingerprints also in the optical spectra. In these regards, since the structure of the polymer is driven, among other factors, by the temperature of the process, it can be guessed that complete polymerization would be achieved at the highest temperatures. Indeed, the studies of Tyborski and coworkers[37, 38] report (process) temperature-dependent UV-vis spectra where, as T increases from 400°C, a sharp reduction of the energy of peak absorption and emission, as well as in the onset (direct) of the optical absorption. The authors attribute such an effect to a change in the inter-layer coupling; instead, we suggest that our results provide an alternative explanation, based on a partial or complete polymerization of the sample.

4. Conclusions

In this work, we performed a computational investigation of the excitonic and vibrational properties of different polymers of melem-based graphitic carbon nitride (gCN). Our aims were to identify unique fingerprints of each polymeric arrangement within optical spectra, to perform a comparison with the properties of the molecular precursor and to identify interesting effects or trends, related for example the layered material thickness or to any constraints imposed to the structural model.

For this purpose, we carried out density functional theory calculations, including hybrid methods, of the fully or partially polymerized gCN and we investigated their optically excited state by approximating the first excited singlet spin-state with the ground triplet spin-state, or in other words the electron-hole pair. We evaluated the interaction between the charge carriers, through the inspection of the electronic charge density and the analysis of the band structure. Additionally, we studied polaronic self-trapping effects, by further optimizing the atomic positions in the presence of the excited charge carriers. We evaluated the exciton binding energy through the hydrogenic approximation and, thus, calculated the effective masses of the charge carriers. This required to evaluate the dielectric constant, which we obtained by two independent models, one analytical and one more macroscopic, also including the ionic contribution to polarization.

https://doi.org/10.1016/j.apsusc.2022.155164

Our results show that, while the single electron and single hole are delocalized on a Π^*/N pyridinic p_z state, the electron-hole pair is bound and is well localized on a single monomer unit in the supercell, independently from the gCN model considered. Irrespective of the type of polymerization, the exciton binding energy in a two-dimensional model is more than doubled with respect to the corresponding bulk structure. We predict that the exciton formed in the 2D systems to be stable, at least at room temperature, and to give rise to an appreciable Stoke-shift between absorption and photoemission spectral maxima. Our calculations also indicate that the energies for the photon absorption and the photon emission are larger for melon than igCN (3.39 vs 2.72 eV and 2.95 vs 2.14 eV, respectively), which reflects their different atomic configuration and structure.

The vibrational simulations (IR spectra) of fully and partially polymerized gCN can be distinguished from the absence/presence, respectively, of two absorption features in the region between 3000-3600 cm^{-1}, which are assigned to the N-H stretching by the residual amino groups, being these unique fingerprints of an incomplete polymerization of the precursor molecules.

We believe that the theoretical spectroscopic characterization of various gCN models summarized above can be a useful guide for the experimentalists to rationalize their findings and determine the type of polymer present in their real samples.

5. Acknowledgments

This research was funded by the Italian Ministry of Education, Universities, and Research (MIUR) through the PRIN 2017-N. 2017NYPHN8 (MADAM) program.

References

[1] A. Thomas, A. Fischer, F. Goettmann, M. Antonietti, J.-O. Müller, R. Schlögl, J. M. Carlsson, Graphitic carbon nitride materials: variation of structure and morphology and their use as metal-free catalysts, J. Mater. Chem. 18 (2008) 4893–4908. doi:10.1039/B800274F.
URL http://dx.doi.org/10.1039/B800274F

[2] Y. Zheng, J. Liu, J. Liang, M. Jaroniec, S. Z. Qiao, Graphitic carbon nitride materials: controllable synthesis and applications in fuel

https://doi.org/10.1016/j.apsusc.2022.155164

cells and photocatalysis, Energy Environ. Sci. 5 (2012) 6717–6731. doi:10.1039/C2EE03479D.
URL http://dx.doi.org/10.1039/C2EE03479D

[3] J. Liu, H. Wang, M. Antonietti, Graphitic carbon nitride "reloaded": emerging applications beyond (photo)catalysis, Chem. Soc. Rev. 45 (2016) 2308–2326. doi:10.1039/C5CS00767D.
URL http://dx.doi.org/10.1039/C5CS00767D

[4] T. S. Miller, A. B. Jorge, T. M. Suter, A. Sella, F. Corà, P. F. McMillan, Carbon nitrides: synthesis and characterization of a new class of functional materials, Phys. Chem. Chem. Phys. 19 (2017) 15613–15638. doi:10.1039/C7CP02711G.
URL http://dx.doi.org/10.1039/C7CP02711G

[5] W. Jiang, H. Wang, X. Zhang, Y. Zhu, Y. Xie, Two-dimensional polymeric carbon nitride: structural engineering for optimizing photocatalysis, Science China Chemistry 61 (2018) 1205–1213. doi:10.1007/s11426-018-9292-7.
URL https://doi.org/10.1007/s11426-018-9292-7

[6] V. W.-h. Lau, B. V. Lotsch, A tour-guide through carbon nitride-land: Structure- and dimensionality-dependent properties for photo(electro)chemical energy conversion and storage, Advanced Energy Materials 12 (4) (2022) 2101078. arXiv:https://onlinelibrary.wiley.com/doi/pdf/10.1002/aenm.202101078, doi:https://doi.org/10.1002/aenm.202101078.
URL https://onlinelibrary.wiley.com/doi/abs/10.1002/aenm.202101078

[7] A. Thomas, A. Fischer, F. Goettmann, M. Antonietti, J.-O. Müller, R. Schlögl, J. M. Carlsson, Graphitic carbon nitride materials: variation of structure and morphology and their use as metal-free catalysts, J. Mater. Chem. 18 (2008) 4893–4908. doi:10.1039/B800274F.
URL http://dx.doi.org/10.1039/B800274F

[8] Y. Wang, X. Wang, M. Antonietti, Polymeric graphitic carbon nitride as a heterogeneous organocatalyst: From photochemistry to multipurpose catalysis to sustainable chemistry, Angewandte Chemie International Edition 51 (1) (2012) 68–89. arXiv:https://onlinelibrary.wiley.com/doi/pdf/10.1002/anie.201101182,

https://doi.org/10.1016/j.apsusc.2022.155164

doi:https://doi.org/10.1002/anie.201101182.
URL https://onlinelibrary.wiley.com/doi/abs/10.1002/anie.201101182

[9] Z. Zhao, Y. Sun, F. Dong, Graphitic carbon nitride based nanocomposites: a review, Nanoscale 7 (2015) 15–37. doi:10.1039/C4NR03008G.
URL http://dx.doi.org/10.1039/C4NR03008G

[10] Y. Zheng, L. Lin, B. Wang, X. Wang, Graphitic carbon nitride polymers toward sustainable photoredox catalysis, Angewandte Chemie International Edition 54 (44) (2015) 12868–12884. arXiv:https://onlinelibrary.wiley.com/doi/pdf/10.1002/anie.201501788, doi:https://doi.org/10.1002/anie.201501788.
URL https://onlinelibrary.wiley.com/doi/abs/10.1002/anie.201501788

[11] J. Wen, J. Xie, X. Chen, X. Li, A review on g-c3n4-based photocatalysts, Applied Surface Science 391 (2017) 72–123, 2nd International Symposium on Energy and Environmental Photocatalytic Materials. doi:https://doi.org/10.1016/j.apsusc.2016.07.030.
URL https://www.sciencedirect.com/science/article/pii/S016943321631457X

[12] J. Wen, J. Xie, X. Chen, X. Li, A review on g-c3n4-based photocatalysts, Applied Surface Science 391 (2017) 72–123, 2nd International Symposium on Energy and Environmental Photocatalytic Materials. doi:https://doi.org/10.1016/j.apsusc.2016.07.030.
URL https://www.sciencedirect.com/science/article/pii/S016943321631457X

[13] P. Kumar, R. Boukherroub, K. Shankar, Sunlight-driven water-splitting using two-dimensional carbon based semiconductors, J. Mater. Chem. A 6 (2018) 12876–12931. doi:10.1039/C8TA02061B.
URL http://dx.doi.org/10.1039/C8TA02061B

[14] M. Majdoub, Z. Anfar, A. Amedlous, Emerging chemical functionalization of g-c3n4: Covalent/noncovalent modifications and applications, ACS Nano 14 (10) (2020) 12390–12469, pMID: 33052050. arXiv:https://doi.org/10.1021/acsnano.0c06116, doi:10.1021/acsnano.0c06116.
URL https://doi.org/10.1021/acsnano.0c06116

[15] K. A. Adegoke, N. W. Maxakato, Efficient strategies for boosting the performance of 2d graphitic carbon nitride nanoma-

https://doi.org/10.1016/j.apsusc.2022.155164

terials during photoreduction of carbon dioxide to energy-rich chemicals, Materials Today Chemistry 23 (2022) 100605. doi:https://doi.org/10.1016/j.mtchem.2021.100605.
URL https://www.sciencedirect.com/science/article/pii/S2468519421001853

[16] G. Gao, Y. Jiao, E. R. Waclawik, A. Du, Single atom (pd/pt) supported on graphitic carbon nitride as an efficient photocatalyst for visible-light reduction of carbon dioxide, Journal of the American Chemical Society 138 (19) (2016) 6292–6297, pMID: 27116595. arXiv:https://doi.org/10.1021/jacs.6b02692, doi:10.1021/jacs.6b02692.
URL https://doi.org/10.1021/jacs.6b02692

[17] S. Lu, C. Li, H. Li, Y. Zhao, Y. Gong, L. Niu, X. Liu, T. Wang, The effects of nonmetal dopants on the electronic, optical and chemical performances of monolayer g–c3n4 by first-principles study, Applied Surface Science 392 (2017) 966–974. doi:https://doi.org/10.1016/j.apsusc.2016.09.136.
URL https://www.sciencedirect.com/science/article/pii/S0169433216320177

[18] B. Zhu, L. Zhang, B. Cheng, J. Yu, First-principle calculation study of tri-s-triazine-based g-c3n4: A review, Applied Catalysis B: Environmental 224 (2018) 983–999. doi:https://doi.org/10.1016/j.apcatb.2017.11.025.
URL https://www.sciencedirect.com/science/article/pii/S0926337317310809

[19] J. Xue, M. Fujitsuka, T. Majima, The role of nitrogen defects in graphitic carbon nitride for visible-light-driven hydrogen evolution, Phys. Chem. Chem. Phys. 21 (2019) 2318–2324. doi:10.1039/C8CP06922K.
URL http://dx.doi.org/10.1039/C8CP06922K

[20] Y. Dai, Y. Gu, Y. Bu, Modulation of the photocatalytic performance of g-c3n4 by two-sites co-doping using variable valence metal, Applied Surface Science 500 (2020) 144036. doi:https://doi.org/10.1016/j.apsusc.2019.144036.
URL https://www.sciencedirect.com/science/article/pii/S0169433219328521

[21] X. Liu, W. Kang, W. Zeng, Y. Zhang, L. Qi, F. Ling, L. Fang, Q. Chen, M. Zhou, Structural, electronic and photocatalytic properties of g-c3n4 with intrinsic defects: A first-principles hybrid

https://doi.org/10.1016/j.apsusc.2022.155164

functional investigation, Applied Surface Science 499 (2020) 143994. doi:https://doi.org/10.1016/j.apsusc.2019.143994.
URL https://www.sciencedirect.com/science/article/pii/S0169433219328107

[22] Z. Wang, E. Almatrafi, H. Wang, H. Qin, W. Wang, L. Du, S. Chen, G. Zeng, P. Xu, Cobalt single atoms anchored on oxygen-doped tubular carbon nitride for efficient peroxymonosulfate activation: Simultaneous coordination structure and morphology modulation, Angewandte Chemie International Edition 61 (29) (2022) e202202338. arXiv:https://onlinelibrary.wiley.com/doi/pdf/10.1002/anie.202202338, doi:https://doi.org/10.1002/anie.202202338.
URL https://onlinelibrary.wiley.com/doi/abs/10.1002/anie.202202338

[23] B. V. Lotsch, M. Döblinger, S. Jan, L. Seyfarth, J. Senker, O. Oeckler, W. Schnick, Unmasking melon by a complementary approach employing electron diffraction, solid-state nmr spectroscopy, and theoretical calculations—structural characterization of a carbon nitride polymer, Chemistry – A European Journal 13 (17) (2007) 4969–4980. arXiv:https://chemistry-europe.onlinelibrary.wiley.com/doi/pdf/10.1002/chem.200601759, doi:https://doi.org/10.1002/chem.200601759.
URL https://chemistry-europe.onlinelibrary.wiley.com/doi/abs/10.1002/chem.200

[24] F. Fina, S. Callear, G. Carins, I. JTS, Structural investigation of graphitic carbon nitride via xrd and neutron diffraction, Chem. Mater. 27 (2015) 2612. doi:10.1021/acs.chemmater.5b00411.

[25] K. Akaike, K. Aoyama, S. Dekubo, A. Onishi, K. Kanai, Characterizing electronic structure near the energy gap of graphitic carbon nitride based on rational interpretation of chemical analysis, Chem. Mater. 30 (2018) 2341. doi:10.1021/acs.chemmater.7b05316.

[26] C. Cometto, A. Ugolotti, E. Grazietti, A. Moretto, G. Bottaro, L. Armelao, L. Di Valentin, Cristiana a nd Calvillo, G. Granozzi, Copper single-atoms embedded in 2d graphitic carbon nitride for the co_2 reduction, npj 2D Materials and Applications 5 (2021) 63. doi:10.1038/s41699-021-00243-y.

[27] A. Ugolotti, C. Di Valentin, Ab-initio spectroscopic characterization of melem-based graphitic carbon nitride polymorphs, Nanomaterials 11 (7)

https://doi.org/10.1016/j.apsusc.2022.155164

(2021). doi:10.3390/nano11071863.
URL https://www.mdpi.com/2079-4991/11/7/1863

[28] B. Jürgens, E. Irran, J. Senker, P. Kroll, H. Müller, W. Schnick, Melem (2,5,8-triamino-tri-s-triazine), an important intermediate during condensation of melamine rings to graphitic carbon nitride: Synthesis, structure determination by x-ray powder diffractometry, solid-state nmr, and theoretical studies, Journal of the American Chemical Society 125 (34) (2003) 10288–10300, pMID: 12926953. arXiv:https://doi.org/10.1021/ja0357689, doi:10.1021/ja0357689.
URL https://doi.org/10.1021/ja0357689

[29] J. Wang, W.-D. Zhang, Modification of tio2 nanorod arrays by graphite-like c3n4 with high visible light photoelectrochemical activity, Electrochimica Acta 71 (2012) 10–16. doi:https://doi.org/10.1016/j.electacta.2012.03.102.
URL https://www.sciencedirect.com/science/article/pii/S0013468612004549

[30] Z. Zeng, X. Quan, H. Yu, S. Chen, Y. Zhang, H. Zhao, S. Zhang, Carbon nitride with electron storage property: Enhanced exciton dissociation for high-efficient photocatalysis, Applied Catalysis B: Environmental 236 (2018) 99–106. doi:https://doi.org/10.1016/j.apcatb.2018.05.003.
URL https://www.sciencedirect.com/science/article/pii/S0926337318304211

[31] Y.-Y. Li, Y. Si, E.-X. Han, W.-Q. Huang, W. Hu, A. Pan, X. Fan, G.-F. Huang, Steering charge kinetics boost the photocatalytic activity of graphitic carbon nitride: heteroatom-mediated spatial charge separation and transfer, Journal of Physics D: Applied Physics 53 (2019) 015502. doi:10.1088/1361-6463/ab48b1.
URL https://doi.org/10.1088/1361-6463/ab48b1

[32] Y. Kang, Y. Yang, L.-C. Yin, X. Kang, L. Wang, G. Liu, H.-M. Cheng, Selective breaking of hydrogen bonds of layered carbon nitride for visible light photocatalysis, Advanced Materials 28 (30) (2016) 6471–6477. arXiv:https://onlinelibrary.wiley.com/doi/pdf/10.1002/adma.201601567, doi:https://doi.org/10.1002/adma.201601567.
URL https://onlinelibrary.wiley.com/doi/abs/10.1002/adma.201601567

[33] A. Zambon, J.-M. Mouesca, C. Gheorghiu, P. A. Bayle, J. Pécaut, M. Claeys-Bruno, S. Gambarelli, L. Dubois, s-heptazine oligomers:

https://doi.org/10.1016/j.apsusc.2022.155164

promising structural models for graphitic carbon nitride, Chem. Sci. 7 (2016) 945–950. doi:10.1039/C5SC02992A.
URL http://dx.doi.org/10.1039/C5SC02992A

[34] G. P. Mane, S. N. Talapaneni, K. S. Lakhi, H. Ilbeygi, U. Ravon, K. Al-Bahily, T. Mori, D.-H. Park, A. Vinu, Highly ordered nitrogen-rich mesoporous carbon nitrides and their superior performance for sensing and photocatalytic hydrogen generation, Angewandte Chemie International Edition 56 (29) (2017) 8481–8485. arXiv:https://onlinelibrary.wiley.com/doi/pdf/10.1002/anie.201702386, doi:https://doi.org/10.1002/anie.201702386.
URL https://onlinelibrary.wiley.com/doi/abs/10.1002/anie.201702386

[35] X. Li, S. T. A. G. Melissen, T. Le Bahers, P. Sautet, A. F. Masters, S. N. Steinmann, T. Maschmeyer, Shining light on carbon nitrides: Leveraging temperature to understand optical gap variations, Chemistry of Materials 30 (2018) 4253–4262. doi:10.1021/acs.chemmater.8b00740.
URL https://doi.org/10.1021/acs.chemmater.8b00740

[36] Y. Ma, F. Liu, Y. Liu, X. Lan, Y. Zhu, J. Shi, W. Jiang, G. Wang, S. H. Park, In-situ intramolecular synthesis of tubular carbon nitride s-scheme homojunctions with exceptional in-plane exciton splitting and mechanism insight, Chemical Engineering Journal 414 (2021) 128802. doi:https://doi.org/10.1016/j.cej.2021.128802.
URL https://www.sciencedirect.com/science/article/pii/S1385894721003995

[37] T. Tyborski, C. Merschjann, S. Orthmann, F. Yang, M.-C. Lux-Steiner, T. Schedel-Niedrig, Tunable optical transition in polymeric carbon nitrides synthesized via bulk thermal condensation, Journal of Physics: Condensed Matter 24 (16) (2012) 162201. doi:10.1088/0953-8984/24/16/162201.
URL https://doi.org/10.1088/0953-8984/24/16/162201

[38] C. Merschjann, T. Tyborski, S. Orthmann, F. Yang, K. Schwarzburg, M. Lublow, M.-C. Lux-Steiner, T. Schedel-Niedrig, Photophysics of polymeric carbon nitride: An optical quasimonomer, Phys. Rev. B 87 (2013) 205204. doi:10.1103/PhysRevB.87.205204.
URL https://link.aps.org/doi/10.1103/PhysRevB.87.205204

https://doi.org/10.1016/j.apsusc.2022.155164

[39] C. Merschjann, S. Tschierlei, T. Tyborski, K. Kailasam, S. Orthmann, D. Hollmann, T. Schedel-Niedrig, A. Thomas, S. Lochbrunner, Complementing graphenes: 1d interplanar charge transport in polymeric graphitic carbon nitrides, Advanced Materials 27 (48) (2015) 7993–7999. arXiv:https://onlinelibrary.wiley.com/doi/pdf/10.1002/adma.201503448, doi:https://doi.org/10.1002/adma.201503448.
URL https://onlinelibrary.wiley.com/doi/abs/10.1002/adma.201503448

[40] H. Wang, S. Jiang, S. Chen, X. Zhang, W. Shao, X. Sun, Z. Zhao, Q. Zhang, Y. Luo, Y. Xie, Insights into the excitonic processes in polymeric photocatalysts, Chem. Sci. 8 (2017) 4087–4092. doi:10.1039/C7SC00307B.
URL http://dx.doi.org/10.1039/C7SC00307B

[41] A. J. Heeger, Semiconducting polymers: the third generation, Chem. Soc. Rev. 39 (2010) 2354–2371. doi:10.1039/B914956M.
URL http://dx.doi.org/10.1039/B914956M

[42] S. Brazovskii, N. Kirova, Physical theory of excitons in conducting polymers, Chem. Soc. Rev. 39 (2010) 2453–2465. doi:10.1039/B917724H.
URL http://dx.doi.org/10.1039/B917724H

[43] X. Wang, K. Maeda, X. Chen, K. Takanabe, K. Domen, Y. Hou, X. Fu, M. Antonietti, Polymer semiconductors for artificial photosynthesis: Hydrogen evolution by mesoporous graphitic carbon nitride with visible light, Journal of the American Chemical Society 131 (5) (2009) 1680–1681, pMID: 19191697. arXiv:https://doi.org/10.1021/ja809307s, doi:10.1021/ja809307s.
URL https://doi.org/10.1021/ja809307s

[44] P. Niu, L. Zhang, G. Liu, H.-M. Cheng, Graphene-like carbon nitride nanosheets for improved photocatalytic activities, Advanced Functional Materials 22 (22) (2012) 4763–4770. arXiv:https://onlinelibrary.wiley.com/doi/pdf/10.1002/adfm.201200922, doi:https://doi.org/10.1002/adfm.201200922.
URL https://onlinelibrary.wiley.com/doi/abs/10.1002/adfm.201200922

[45] F. Dong, Y. Li, Z. Wang, W.-K. Ho, Enhanced visible light photocatalytic activity and oxidation ability of porous graphene-like g-c3n4 nanosheets via thermal exfoliation, Applied Surface Science

https://doi.org/10.1016/j.apsusc.2022.155164

358 (2015) 393–403, graphene and C3N4-based Photocatalysts. doi:https://doi.org/10.1016/j.apsusc.2015.04.034.
URL https://www.sciencedirect.com/science/article/pii/S0169433215008740

[46] Z. Gan, Y. Shan, J. Chen, Q. Gui, Q. Zhang, S. Nie, X. Wu, The origins of the broadband photoluminescence from carbon nitrides and applications to white light emitting, Nano Research 9 (2016) 1801–1812. doi:10.1007/s12274-016-1073-2.
URL https://doi.org/10.1007/s12274-016-1073-2

[47] P. Niu, H. Li, Y. Ma, T. Zhai, Extended visible light absorption combined with promoted charge carrier transfer in urea-derived graphitic carbon nitride for enhanced photocatalytic hydrogen evolution performances, The Journal of Physical Chemistry C 122 (36) (2018) 20717–20726. arXiv:https://doi.org/10.1021/acs.jpcc.8b04849, doi:10.1021/acs.jpcc.8b04849.
URL https://doi.org/10.1021/acs.jpcc.8b04849

[48] H. Zhang, X. Zuo, H. Tang, G. Li, Z. Zhou, Origin of photoactivity in graphitic carbon nitride and strategies for enhancement of photocatalytic efficiency: insights from first-principles computations, Phys. Chem. Chem. Phys. 17 (2015) 6280–6288. doi:10.1039/C4CP05288A.
URL http://dx.doi.org/10.1039/C4CP05288A

[49] W. Wei, T. Jacob, Strong excitonic effects in the optical properties of graphitic carbon nitride g-c_3n_4 from first principles, Phys. Rev. B 87 (2013) 085202. doi:10.1103/PhysRevB.87.085202.
URL https://link.aps.org/doi/10.1103/PhysRevB.87.085202

[50] G. A. Meek, A. D. Baczewski, D. J. Little, B. G. Levine, Polaronic relaxation by three-electron bond formation in graphitic carbon nitrides, The Journal of Physical Chemistry C 118 (8) (2014) 4023–4032. arXiv:https://doi.org/10.1021/jp412305y, doi:10.1021/jp412305y.
URL https://doi.org/10.1021/jp412305y

[51] S. Melissen, T. Le Bahers, S. N. Steinmann, P. Sautet, Relationship between carbon nitride structure and exciton binding energies: A dft perspective, The Journal of Physical Chemistry C 119 (45) (2015) 25188–25196. arXiv:https://doi.org/10.1021/acs.jpcc.5b07059,

https://doi.org/10.1016/j.apsusc.2022.155164

doi:10.1021/acs.jpcc.5b07059.
URL https://doi.org/10.1021/acs.jpcc.5b07059

[52] W. F. Espinosa-García, J. M. Osorio-Guillén, C. M. Araujo, Dimension-dependent band alignment and excitonic effects in graphitic carbon nitride: a many-body perturbation and time-dependent density functional theory study, RSC Adv. 7 (2017) 44997–45002. doi:10.1039/C7RA07134E.
URL http://dx.doi.org/10.1039/C7RA07134E

[53] K. L. Corp, C. W. Schlenker, Ultrafast spectroscopy reveals electron-transfer cascade that improves hydrogen evolution with carbon nitride photocatalysts, Journal of the American Chemical Society 139 (23) (2017) 7904–7912, pMID: 28535670. arXiv:https://doi.org/10.1021/jacs.7b02869, doi:10.1021/jacs.7b02869.
URL https://doi.org/10.1021/jacs.7b02869

[54] A. Becke, Density-functional thermochemistry. iii. the role of exact exchange, J. Chem. Phys. 98 (1993) 5648. doi:10.1063/1.464913.

[55] C. Lee, W. Yang, R. G. Parr, Development of the colle-salvetti correlation-energy formula into a functional of the electron density, Phys. Rev. B 37 (1988) 785–789. doi:10.1103/PhysRevB.37.785.
URL https://link.aps.org/doi/10.1103/PhysRevB.37.785

[56] S. Grimme, J. Antony, S. Ehrlich, H. Krieg, A consistent and accurate ab initio parametrization of density functional dispersion correction (dft-d) for the 94 elements h-pu, The Journal of Chemical Physics 132 (15) (2010) 154104. doi:10.1063/1.3382344.

[57] P. Cudazzo, I. V. Tokatly, A. Rubio, Dielectric screening in two-dimensional insulators: Implications for excitonic and impurity states in graphane, Phys. Rev. B 84 (2011) 085406. doi:10.1103/PhysRevB.84.085406.
URL https://link.aps.org/doi/10.1103/PhysRevB.84.085406

[58] T. Olsen, S. Latini, F. Rasmussen, K. S. Thygesen, Simple screened hydrogen model of excitons in two-dimensional materials, Phys. Rev. Lett. 116 (2016) 056401. doi:10.1103/PhysRevLett.116.056401.
URL https://link.aps.org/doi/10.1103/PhysRevLett.116.056401

https://doi.org/10.1016/j.apsusc.2022.155164

[59] A. Laturia, M. L. Van de Put, W. G. Vandenberghe, Dielectric properties of hexagonal boron nitride and transition metal dichalcogenides: from monolayer to bulk, npj 2D Materials and Applications 2 (2018) 6. doi:10.1038/s41699-018-0050-x.
URL https://doi.org/10.1038/s41699-018-0050-x

[60] T. Tian, D. Scullion, D. Hughes, L. H. Li, C.-J. Shih, J. Coleman, M. Chhowalla, E. J. G. Santos, Electronic polarizability as the fundamental variable in the dielectric properties of two-dimensional materials, Nano Letters 20 (2) (2020) 841–851, pMID: 31888332. arXiv:https://doi.org/10.1021/acs.nanolett.9b02982, doi:10.1021/acs.nanolett.9b02982.
URL https://doi.org/10.1021/acs.nanolett.9b02982

[61] R. Dovesi, V. R. Saunders, C. Roetti, R. Orlando, C. M. Zicovich-Wilson, F. Pascale, B. Civalleri, K. Doll, N. M. Harrison, I. J. Bush, P. D'Arco, M. Llunell, M. Causà, Y. Noël, L. Maschio, A. Erba, M. Rerat, S. Casassa, CRYSTAL17 User's Manual, University of Torino, Torino, 2017.

[62] R. Dovesi, A. Erba, R. Orlando, C. M. Zicovich-Wilson, B. Civalleri, L. Maschio, M. Rérat, S. Casassa, J. Baima, S. Salustro, B. Kirtman, Quantum-mechanical condensed matter simulations with crystal, WIREs Computational Molecular Science 8 (4) (2018) e1360. arXiv:https://wires.onlinelibrary.wiley.com/doi/pdf/10.1002/wcms.1360, doi:https://doi.org/10.1002/wcms.1360.
URL https://wires.onlinelibrary.wiley.com/doi/abs/10.1002/wcms.1360

[63] C. Gatti, V. R. Saunders, C. Roetti, Crystal field effects on the topological properties of the electron density in molecular crystals: The case of urea, The Journal of Chemical Physics 101 (12) (1994) 10686–10696. arXiv:https://doi.org/10.1063/1.467882, doi:10.1063/1.467882.
URL https://doi.org/10.1063/1.467882

[64] J. Heyd, G. E. Scuseria, M. Ernzerhof, Hybrid functionals based on a screened coulomb potential, The Journal of Chemical Physics 118 (18) (2003) 8207–8215. arXiv:https://doi.org/10.1063/1.1564060, doi:10.1063/1.1564060.
URL https://doi.org/10.1063/1.1564060

https://doi.org/10.1016/j.apsusc.2022.155164

[65] J. Heyd, G. E. Scuseria, M. Ernzerhof, Erratum: "hybrid functionals based on a screened coulomb potential" [j. chem. phys. 118, 8207 (2003)], The Journal of Chemical Physics 124 (21) (2006) 219906. arXiv:https://doi.org/10.1063/1.2204597, doi:10.1063/1.2204597.
URL https://doi.org/10.1063/1.2204597

[66] C. Adamo, V. Barone, Toward reliable density functional methods without adjustable parameters: The pbe0 model, The Journal of Chemical Physics 110 (13) (1999) 6158–6170. arXiv:https://doi.org/10.1063/1.478522, doi:10.1063/1.478522.
URL https://doi.org/10.1063/1.478522

[67] C. Di Valentin, A. Selloni, Bulk and surface polarons in photoexcited anatase tio2, The Journal of Physical Chemistry Letters 2 (17) (2011) 2223–2228. arXiv:https://doi.org/10.1021/jz2009874, doi:10.1021/jz2009874.
URL https://doi.org/10.1021/jz2009874

[68] H. Liu, P. Lazzaroni, C. Di Valentin, Nature of excitons in bidimensional wse2 by hybrid density functional theory calculations, Nanomaterials 8 (7) (2018). doi:10.3390/nano8070481.
URL https://www.mdpi.com/2079-4991/8/7/481

[69] T. Le Bahers, M. Rérat, P. Sautet, Semiconductors used in photovoltaic and photocatalytic devices: Assessing fundamental properties from dft, The Journal of Physical Chemistry C 118 (12) (2014) 5997–6008. arXiv:https://doi.org/10.1021/jp409724c, doi:10.1021/jp409724c.
URL https://doi.org/10.1021/jp409724c

[70] X. Gonze, C. Lee, Dynamical matrices, born effective charges, dielectric permittivity tensors, and interatomic force constants from density-functional perturbation theory, Phys. Rev. B 55 (1997) 10355–10368. doi:10.1103/PhysRevB.55.10355.
URL https://link.aps.org/doi/10.1103/PhysRevB.55.10355

[71] M. Ferrero, M. Rérat, R. Orlando, R. Dovesi, Coupled perturbed hartree-fock for periodic systems: The role of symmetry and related computational aspects, The Journal of Chemical Physics 128 (1) (2008) 014110. arXiv:https://doi.org/10.1063/1.2817596,

https://doi.org/10.1016/j.apsusc.2022.155164

doi:10.1063/1.2817596.
URL https://doi.org/10.1063/1.2817596

[72] M. Ferrero, M. Rérat, R. Orlando, R. Dovesi, The calculation of static polarizabilities of 1-3d periodic compounds. the implementation in the crystal code, Journal of Computational Chemistry 29 (9) (2008) 1450–1459. arXiv:https://onlinelibrary.wiley.com/doi/pdf/10.1002/jcc.20905, doi:https://doi.org/10.1002/jcc.20905.
URL https://onlinelibrary.wiley.com/doi/abs/10.1002/jcc.20905

[73] M. Ferrero, M. Rérat, B. Kirtman, R. Dovesi, Calculation of first and second static hyperpolarizabilities of one- to three-dimensional periodic compounds. implementation in the crystal code., The Journal of Chemical Physics 129 (24) (2008) 244110. arXiv:https://doi.org/10.1063/1.3043366, doi:10.1063/1.3043366.
URL https://doi.org/10.1063/1.3043366

[74] M. J. Frisch, G. W. Trucks, H. B. Schlegel, G. E. Scuseria, M. A. Robb, J. R. Cheeseman, G. Scalmani, V. Barone, G. A. Petersson, H. Nakatsuji, X. Li, M. Caricato, A. V. Marenich, J. Bloino, B. G. Janesko, R. Gomperts, B. Mennucci, H. P. Hratchian, J. V. Ortiz, A. F. Izmaylov, J. L. Sonnenberg, D. Williams-Young, F. Ding, F. Lipparini, F. Egidi, J. Goings, B. Peng, A. Petrone, T. Henderson, D. Ranasinghe, V. G. Zakrzewski, J. Gao, N. Rega, G. Zheng, W. Liang, M. Hada, M. Ehara, K. Toyota, R. Fukuda, J. Hasegawa, M. Ishida, T. Nakajima, Y. Honda, O. Kitao, H. Nakai, T. Vreven, K. Throssell, J. Montgomery, J. A., J. E. Peralta, F. Ogliaro, M. J. Bearpark, J. J. Heyd, E. N. Brothers, K. N. Kudin, V. N. Staroverov, T. A. Keith, R. Kobayashi, J. Normand, K. Raghavachari, A. P. Rendell, J. C. Burant, S. S. Iyengar, J. Tomasi, M. Cossi, J. M. Millam, M. Klene, C. Adamo, R. Cammi, J. W. Ochterski, R. L. Martin, K. Morokuma, O. Farkas, J. B. Foresman, D. J. Fox, Gaussian 16, Revision C.01,, Gaussian, Inc., Wallingford CT, 2016.

[75] P. Ugliengo, F. Pascale, M. Mérawa, P. Labéguerie, S. Tosoni, R. Dovesi, Infrared spectra of hydrogen-bonded ionic crystals: Ab initio study of $Mg(OH)_2$ and β-$Be(OH)_2$, The Journal of Physical Chemistry B 108 (36) (2004) 13632–13637. arXiv:https://doi.org/10.1021/jp047514v, doi:10.1021/jp047514v.
URL https://doi.org/10.1021/jp047514v

https://doi.org/10.1016/j.apsusc.2022.155164

[76] F. Pascale, S. Tosoni, C. Zicovich-Wilson, P. Ugliengo, R. Orlando, R. Dovesi, Vibrational spectrum of brucite, $Mg(OH)_2$: a periodic ab initio quantum mechanical calculation including OH anharmonicity, Chemical Physics Letters 396 (4) (2004) 308–315. doi:https://doi.org/10.1016/j.cplett.2004.08.047.
URL https://www.sciencedirect.com/science/article/pii/S0009261404012436

[77] M. Re Fiorentin, F. Risplendi, M. Palummo, G. Cicero, First-principles calculations of exciton radiative lifetimes in monolayer graphitic carbon nitride nanosheets: Implications for photocatalysis, ACS Applied Nano Materials 4 (2) (2021) 1985–1993. arXiv:https://doi.org/10.1021/acsanm.0c03317, doi:10.1021/acsanm.0c03317.
URL https://doi.org/10.1021/acsanm.0c03317

[78] X. Zhang, X. Xie, H. Wang, J. Zhang, B. Pan, Y. Xie, Enhanced photoresponsive ultrathin graphitic-phase c3n4 nanosheets for bioimaging, Journal of the American Chemical Society 135 (1) (2013) 18–21, pMID: 23244197. arXiv:https://doi.org/10.1021/ja308249k, doi:10.1021/ja308249k.
URL https://doi.org/10.1021/ja308249k

https://doi.org/10.1016/j.apsusc.2022.155164